Anisotropic Forbush decrease of 24 March 2024: First look

Alexander Mishev [a,*], Nicholas Larsen [a], Eleanna Asvestari [b], Alejandro Sáiz [c],
Margaret Ann Shea [d], Du Toit Strauss [e], David Ruffolo [c], Chanoknan Banglieng [f],
Surujhdeo Seunarine [g], Marc L. Duldig [h], Agnieszka Gil [i], Juan José Blanco [j],
Oscar García-Población [j], Pablo Cervino-Solana [j], James H. Adams, Jr. [k], Ilya Usoskin [l]

[a] *Sodankylä Geophysical Observatory, University of Oulu, Linnanmaa, Oulu 90014, Finland*
[b] *Department of Physics, University of Helsinki, Yliopistonkatu 4, Helsinki 00100, Finland*
[c] *Department of Physics, Faculty of Science, Mahidol University, Bangkok 10400, Thailand*
[d] *100, Tennyson Avenue, Nashua NH 03062, USA*
[e] *Centre for Space Research, North-West University, 11 Hoffmanstreet, Potchefstroom 2531, South Africa*
[f] *Division of Physics, Faculty of Science and Technology, Rajamangala University of Technology Thanyaburi, Pathum Thani 12110, Thailand*
[g] *Department of Physics, University of Wisconsin River Falls, River Falls, WI 54022, USA*
[h] *School of Natural Sciences, University of Tasmania, Hobart, Tasmania 7001, Australia*
[i] *University of Siedlce, Stanisława Konarskiego 2, Siedlce 08-110, Poland*
[j] *Space Research Group, University of Alcalá, Plaza San Diego s/n, Alcalá de Henares, Madrid 28801, Spain*
[k] *Center for Space Plasma and Aeronomic Research, University of Alabama in Huntsville, 301 Sparkman Drive, Huntsville, AL 35899, USA*
[l] *Space Physics and Astronomy Research Unit, University of Oulu, Linnanmaa, Oulu 90014, Finland*

Abstract

A strong Forbush decrease, i.e., suppression of the flux of galactic cosmic rays recorded on Earth, was observed by the global network of ground-based neutron monitors (NMs) on 24–25 March 2024. The decrease was very unusual as characterised by so rapid recovery that a false Ground-level enhancement (GLE) alarm was produced by the corresponding warning systems. Here we present the first comprehensive collection and analysis of the available data for this event. The event was highly anisotropic as exhibited in a 3-h spread of the deep-phase timing for different NMs. The anisotropy was focused nearly at the anti-sunward direction with a narrow cone of $20-30°$. The heliospheric situation leading to this unusual Forbush decrease was quite complex. An analysis of first look records was performed, considering the stations acceptance, taking into account the complex geomagnetic conditions. A leader fraction analysis indicates that the recovery phase of the event was rigidity-independent and had essentially the same spectral shape as the pre-event period. A summary of the solar-terrestrial phenomena is provided to assist in future work on modelling this complex event.
© 2024 COSPAR. Published by Elsevier B.V. This is an open access article under the CC BY license (http://creativecommons.org/licenses/by/4.0/).

Keywords: Cosmic rays; Forbush decrease; Neutron monitor network; Anisotropy

1. Introduction

An omnipresent flux of high-energy subatomic particles, namely protons ($\sim$90%), α-particles ($\sim$9%), and smaller amounts of heavier nuclei constantly bombard the Earth's atmosphere. These particles are of extra-terrestrial and extra-solar, mostly Galactic, origin and are collectively called galactic cosmic rays (GCRs). Their energy spectrum is roughly a power law from about 10^9 to over 10^{20} eV, yet showing a complicated shape and temporal modulation at lower energies (e.g. Dorman, 2004; Gaisser et al., 2016;

---

* Corresponding author.
 E-mail address: alexander.mishev@oulu.fi (A. Mishev).

Tanabashi et al., 2018, and references therein). Their flux, spectrum, and energy composition are measured with high precision in space, e.g., by PAMELA (Payload for Anti-matter Matter Exploration and Light-nuclei Astrophysics – e.g., Adriani et al., 2017) and AMS-02 (Alpha Magnetic Spectrometer – Aguilar et al., 2021a) space-borne detectors. Variability of the energy-integrated GCR intensity is continuously measured by the worldwide network of neutron monitors (NMs) located around the globe (e.g., Bieber et al., 2004; Mavromichalaki et al., 2011; Väisänen et al., 2021). NMs are ground-based detectors measuring the nucleonic component of the cosmic-ray-induced atmospheric cascade (e.g., Simpson, 2000) and provide accurate monitoring of the GCR flux in the energy range of deka-GeV most affected by solar modulation (Asvestari et al., 2017).

The flux of GCRs is nearly isotropic and varies at different timescales due to heliospheric modulation by the solar wind and embedded interplanetary magnetic field (e.g., Potgieter, 2013, and references therein). In addition to the pronounced 11/22-year solar activity/magnetic cycle modulation, the GCR flux also exhibits notable transient suppressions due to coronal mass ejections (CMEs) and co-rotating interaction regions (CIRs) in the solar wind, called Forbush decreases (FDs – e.g., Forbush, 1937; Cane, 2000; Dumbović et al., 2022). FDs strongly affect GCRs in the GeV – deka-GeV energy range, occurring on the timescale of hours to days and are caused by interplanetary shocks and/or magnetic flux ropes passing near the Earth (see, e.g., Cane, 2000; Kuwabara et al., 2009, and discussions therein). They are observed as relatively fast (within a few hours), sometimes two-step, decreases in the count rate of NMs, which can reach 25–30%, (e.g., Gopalswamy et al., 2005; Witasse et al., 2017). The decrease is usually followed by a slow gradual recovery taking up to several days or even a week, with a pronounced diurnal variability due to cosmic ray anisotropy. Strong FDs are often accompanied by major magnetospheric storms (e.g., Belov, 2009, and the discussion threin) and/ or by strong solar energetic particle (SEP) events (e.g., Desai and Giacalone, 2016; Klein and Dalla, 2017; Reames, 2017) including ground-level enhancements (GLEs).

Here we report and analyse a strong FD recently observed by the global NM network during 24–25 March 2024. The event exhibited notable features, such as a rapid recovery that triggered a false alarm in a GLE warning system, i.e., GLE Alert++ (https://swe.ssa.esa.int/web/guest/anemos-federated) (Souvatzoglou et al., 2014; Mavromichalaki et al., 2024) issued three alert emails between 01:37 and 02:47 UT on 25-Mar-2024 (H. Mavromichalaki, personal communication, 2024), while another alarm system at the Bartol Research Institute, University of Delaware USA (https://www.bartol.udel.edu/mangeard/glealarm/index.html) (Kuwabara et al., 2006a; Kuwabara et al., 2006b), issued a warning but not an alert. The event was also highly anisotropic; it had a

deep phase that appeared with a time difference of several hours, as observed by different NMs.

In Section 2, we present the records from the global NM network. In Section 3 we summarize the state of the Earth's magnetosphere and perform the corresponding NM acceptance-cone modelling. In Section 4 we present the state of the heliosphere, and in Section 5, we discuss the observations and plausible phenomenology.

2. Records from the global neutron monitor network

Here we used count-rate and timing records from the global network of NMs (e.g., Simpson, 2000; Dorman, 2004; Ruffolo et al., 2016, and references therein). NMs are standard ground-based cosmic-ray detectors introduced during the International Geophysical Year (IGY) 1957–1958 and specifically designed to monitor CR variations (Simpson, 1958), yet several stations were installed earlier for test purposes (Simpson et al., 1953) as were pilot non-standard detectors (e.g., Adams, 1950). Later, in 1964, the design of the NM was considerably improved, leading to the introduction of the next-generation standard device, conventionally called NM64, or super-monitor (Hatton and Carmichael, 1964). The NM64 super-monitor is a standard detector in the global NM network (e.g., Simpson, 2000; Bütikofer, 2018, and references therein), while a few older IGY NMs are still being used. There was a Soviet analogue of the NM64, called SNM15, which has slightly lower efficiency and is common in the countries of the former USSR and East Europe (e.g., Gil et al., 2015). The records of the bulk of NMs are archived in nearly real-time and available via web-based services (Väisänen et al., 2021), such as the international NM database NMDB (https://nmdb.eu – see, e.g., Mavromichalaki et al., 2011).

NMs detect atmospheric secondary particles (mostly neutrons) generated by interactions of primary cosmic ray ions in the atmosphere. The trajectory of a charged particle with momentum p and charge q in a magnetic field, such as the geomagnetic field, is determined by its rigidity $P = pc/q$. Therefore, for a cosmic ray ion to reach a given location on Earth, from a given direction, its rigidity must exceed a certain cutoff (threshold) rigidity, P_c. The effective vertical cutoff rigidity varies from ~17 GV in parts of Southeast Asia to nearly 0 GV in polar regions. In addition, a kinetic energy of about 430 MeV/n (Miroshnichenko, 2018; Mishev and Poluianov, 2021) known as the atmospheric cutoff is required for a cosmic ray ion to generate a shower that can be detected at ground level. Therefore, polar neutron monitors with $P_c \lesssim 1$ GV have a response determined by the atmospheric cutoff, which depends only on the altitude above sea level of the detector's location. Besides, an NM is characterized by the asymptotic direction, i.e., the sky-projected direction from which a CR particle should arrive to reach the given location on Earth (e.g., Bütikofer, 2018). We emphasize that the sub-network of polar NMs, called Spaceship

Earth, possesses greater sensitivity to anisotropy and transient variations of CR flux compared to NMs at lower latitudes (e.g., Bieber et al., 2004; Mishev and Usoskin, 2020). Hence, a NM station is sensitive to a given segment of the sky, which is specifically important to study anisotropic transient variations in the CR spectrum.

Here we have collected and analyzed available count-rates and neutron timing records for NMs around the globe, from the tropics to polar regions, for the period between 24–25 March 2024 (days of year, DOY 84 and 85). The list of NMs with the effective vertical cutoff rigidities ranging from zero to about 17 GV is given in Table 1 with the data sources indicated. The count rates of all NMs are examined with a 10-min time resolution, corrected for the barometric pressure and efficiency.

In contrast to typical FDs, this event exhibited a rapid (within several hours) recovery of the NM count rate, an anisotropic response as detected by NMs, and a notable shift of the deep phase and recovery between different NMs. The normalized count rates for the NMs studied here are shown in Fig. 1 for 24–25 March. The magnitude of the FD inversely depended on the NM's geomagnetic cutoff rigidity so that the strongest suppression was observed for polar NMs, as expected (see Table 1 and Fig. 9). Furthermore, as all NMs with geomagnetic cutoff $\lesssim 1$ GV are subject to the same atmospheric cutoff that depends only on altitude, the variable suppression must be attributed to the altitude (especially for Dome C and South Pole) or anisotropy affects due to different asymptotic look directions of different NMs. Unusually, different NMs recorded the deep phase at different times: while most of the NMs recorded the maximum magnitude of the FD at around 22 UT on 24 March, henceforth denoted as Phase I, some other NMs (e.g., SOPO, SNAE, AATB, IRK3, MXCO) reached it later, around 01 UT on 25 March, denoted as Phase II. A more detailed analysis is presented below.

To study this FD using NM data, we explicitly considered the magnetospheric conditions and NM acceptance cones, which are necessary for understanding the aniso-

Table 1
List (arranged via ascending order of the geomagnetic cutoff rigidity P_c) of neutron monitors used in this study. Columns represent the site's name; standard acronym; detector type; vertical cutoff rigidity at the time of the FD (in GV); effective energy E_{eff} (in GeV – Alanko et al., 2003; Asvestari et al., 2017); altitude (in meters a.s.l.); geographical latitude and longitude (in degrees); magnitude M of the FD for phases I and II, respectively, in percentage compared to the pre-event CR intensity; the source of data: (1) – NMDB (nmdb.eu), (2) – Oulu site (cosmicrays.oulu.fi), (3) – North-West University (https://fskbhe1.puk.ac.za/neutronmonitor/ and https://natural-sciences.nwu.ac.za/neutron-monitor-data); (4) – Mahidol University; (5) University of Alcalá.

| Name	Acronym	Type	P_c	E_{eff}	Altitude	Lat	Lon	M_I	M_{II}	Source
Inuvik	INVK	18NM64	0.0	11.7	21	68.36	−133.72	7	4	(1)
JangBogo	JBGO	5NM64	0.0	11.7	29	−74.6	164.2	12	12	(1)
Tixie Bay	TXBY	18NM64	0.0	11.7	0	71.6	128.9	11	11	(1)
Fort Smith	FSMT	18NM64	0.12	11.7	21	60.02	−111.93	11	8	(1)
Peawanuck	PWNK	18NM64	0.12	11.7	53	55	−85.4	10	7	(1)
Terre Adelie	TERA	9NM64	0.12	11.7	32	−66.7	140	8	6	(1)
Thule	THUL	9NM64	0.14	11.7	260	76.6	−68.4	9	7	(1)
Dome C	DOMC	Mini-NM	0.21	11.7	3233	−75.1	123.3	16	10	(2)
Oulu	OULU	9NM64	0.21	11.7	15	65.1	25.5	16	9	(2)
SANAE	SNAE	3NM64	0.24	11.7	856	−70.47	4.24	13	15	(3)
Mawson	MWSN	18NM64	0.25	11.8	30	−67.6	62.88	13	6	(1)
Apatity	APTY	18NM64	0.26	11.8	177	67.6	33.3	15	10	(1)
South Pole	SOPO	3NM64	0.35	11.8	2820	−90	–	10	18	(1)
Nain	NAIN	18NM64	0.39	11.8	46	56.6	−61.7	11	7	(1)
Kerguelen	KERG	18NM64	0.53	11.8	0	−49.4	70.3	11	6	(1)
Calgary	CALG	3NM64	0.66	11.8	1123	51.08	−114.13	11	9	(1)
Yakutsk	YKKT	18NM64	0.9	11.9	105	62.03	129.73	13	9	(1)
Kiel	KIEL	18NM64	1.84	12.0	54	54.34	10.12	12	9	(1)
Livingston Island	ORCA	3NM64	1.97	12.1	15	-62.66	−60.39	9	13	(5)
Newark	NEWK	9NM64	2.38	12.5	50	39.68	−75.75	12	12	(1)
Dourbes	DRBS	9NM64	2.93	12.9	225	50.1	4.6	10	5	(1)
Irkutsk3	IRK3	6NM64	3.01	13.0	3000	51.29	100.55	7	9	(1)
Lomnický Štit	LMKS	8SNM15	3.25	13.2	2634	49.2	20.22	10	10	(1)
Jungfraujoch	JUNG1	3NM64	4.22	14.1	3475	46.55	7.98	12	7	(1)
Baksan	BKSN	6NM64	5.29	15.5	1700	43.28	46.69	8	6	(1)
Alma-Ata B	AATB	18NM64	5.61	15.9	3340	43.13	76.55	7	8	(1)
Rome	ROME	17NM64	5.88	16.3	60	41.9	12.52	6	4	(1)
Castilla-La Mancha	CALM	12NM64	6.12	16.7	708	40.4	3.9	6	6	(1)
Potchefstroom	PFTM	8IGY	6.9	17.9	1351	−26.69	27.09	8	10	(3)
Mexico City	MXCO	6NM64	7.28	18.4	2274	19.33	−99.2	6	10	(1)
Athens	ATHN	6NM64	8.15	19.9	260	37.97	23.78	6	4	(1)
Tenerife	ICaRO	3NM64	12.1	27.1	2373	28.3	−16.48	7	3	(5)
Princess Sirindhorn	PSNM	18NM64	16.6	36.1	2560	18.59	98.5	3.0	2.6	(4)
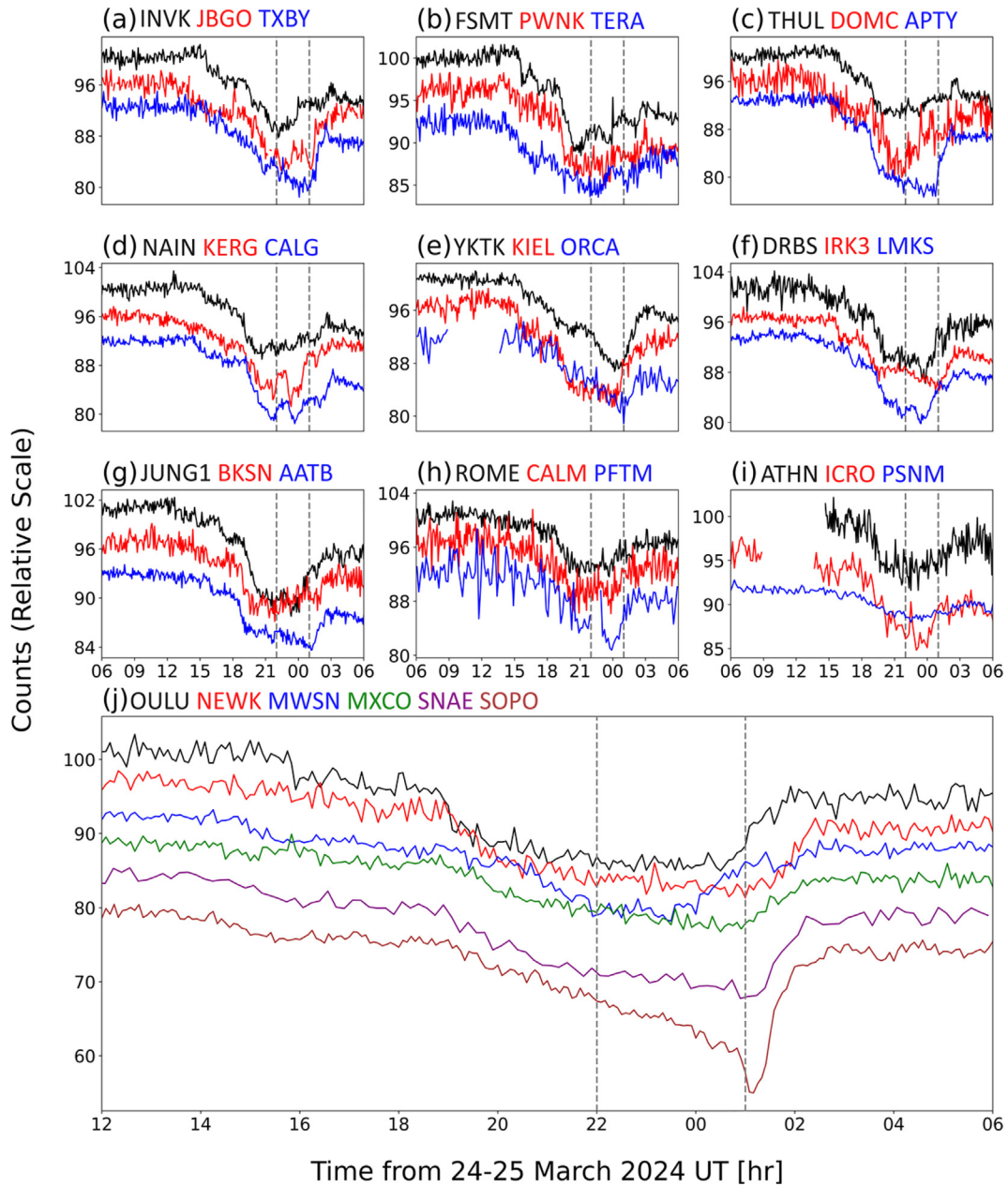
Fig. 1. Normalized count rates of the NMs studied here during the Forbush decrease on 24–25 March 2024. The curves were slightly offset for the sake of visibility. The bottom panel (j) zooms into emphasize the difference in the timing of the deep phase. Phases I and II are denoted by the gray dashed lines.

tropy effects. For that, we modelled the NM acceptance by computing the asymptotic directions and cutoff rigidities of the considered NMs as presented in Section 3.

3. State of the geomagnetosphere and NM asymptotic direction modeling

Realistic modelling of charged particle propagation in the geomagnetosphere is challenging, specifically during significant disturbances, because of the complex dynamical magnetic environment responding to changing near-Earth space conditions (Bütikofer, 2018). A standard approach is that the geomagnetosphere can be realistically described

as a superposition of internal and external magnetic fields, where the former is created by the geodynamo process and the latter by the complex current system in the magnetosphere formed as an interface between the internal field and the interplanetary magnetic field and solar wind plasma. For the internal field, it is usual to employ the International Geomagnetic Reference Field IGRF (e.g., Alken et al., 2021), whilst for the external field one of Tsyganenko models (e.g., see the discussion in Bütikofer, 2018) is often used.

The FD of 24–25 March 2024 occurred during a major geomagnetic storm with planetary K_p index of about 8 for several hours prior to the FD onset (for details see Fig. 2).

Therefore, the particle propagation in the geomagnetosphere was simulated using a combination of the IGRF for the internal and Tsyganenko 01 (Tsyganenko, 2002) model for the external fields, respectively, because the latter is recommended for use when $K_p \geqslant 6$. We used a new tool for the computation of propagation of charged particles in the geomagnetosphere: the Open-source geomagnetosphere propagation tool (OTSO – for details see Larsen et al., 2023). The Tsyganenko 01 model requires several inputs, namely dynamic pressure, solar wind speed, Dst index, B_y and B_z components of the interplanetary magnetic field (IMF), and G1 and G2 values. The latter quantities are used specifically for the Tsyganenko 01 parameterization and are computed using geomagnetic data for the hour preceding the event (for details see Tsyganenko, 2002). The model parameters are given for Phases I and II, summarized in Table 2.

Data for the geomagnetospheric conditions for this FD were collected from various sources. Solar wind data were obtained from the National Oceanic and Atmospheric Administration (NOAA – www.ngdc.noaa.gov/), where data are combined from the Deep Space Climate Observatory (DSCOVR) and the Advanced Composition Explorer (ACE) for solar wind measurements; Dst index from the World Data Center for Geomagnetism Kyoto (https://wdc.kugi.kyoto-u.ac.jp/); and K_p index from GFZ-Potsdam (https://kp.gfz-potsdam.de/en/).

As mentioned above, NMs register particles from a specific segment of the sky, quantified by the asymptotic directions of the station. Asymptotic directions of selected polar NMs during the FD for both phases are presented in Fig. 3 for Phase I (22 UT on 24-Mar-2024) and Phase II (01 UT on 25-Mar-2024), respectively. The asymptotic directions are plotted in geocentric solar ecliptic (GSE) coordi-
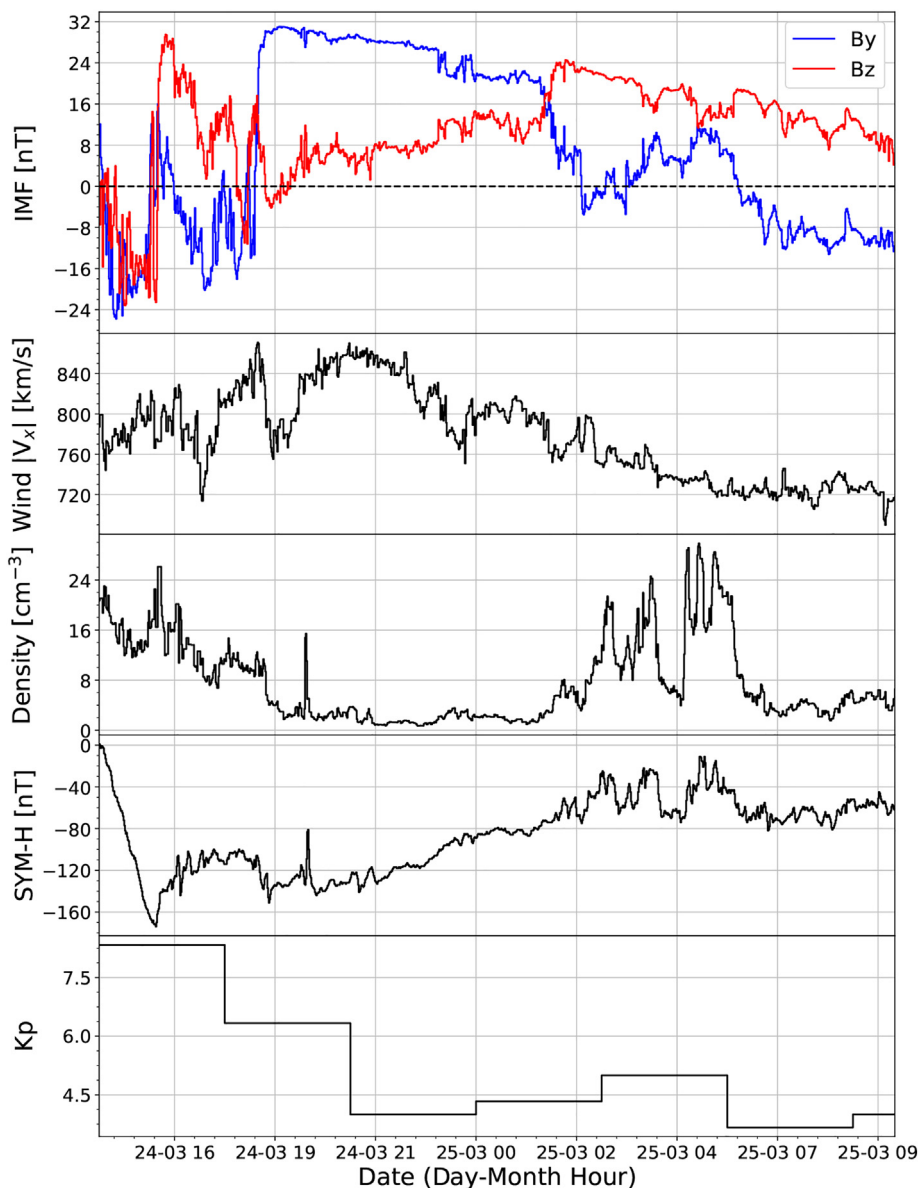

Fig. 2. Indicators of solar wind (upper three panels) and geomagnetospheric (lower two panels) conditions over the period of the FD studied here.

Table 2
Inputs for the Tsyganenko 01 model, namely V_x in km s^{-1}, B_y and B_z in nT, P_{dyn} in nPa, Dst in nT, G1 and G2 = 0.

Phase	V_x	B_y	B_z	P_{dyn}	Dst	G1	G2
Phase I, (22 UT on 24 March 2024)	829.9	16.8	21.2	0.6	−122.0	8.0	0
Phase II, (01 UT on 25 March 2024)	797.5	8.2	18.3	3.9	−94.0	1.21	0

nates to better present the sensitivity of the NM network to local anisotropy. We emphasize that there is a notable change in the asymptotic directions of the stations, due to both variation of the geomagnetic conditions and Earth's rotation. We present asymptotic directions only from several selected polar NMs, in the rigidity range 1–20 GV, whilst in the analysis we used all the stations from Table 1. We note that this rigidity range is representative of the expected response of NMs during FDs. One can see that the coverage of the NM network is relatively good, and allows one to study eventual anisotropy during the FD, see Fig. 3.

4. Associated eruption at the Sun and near-Earth heliospheric conditions

During the days preceding the FD, the Sun was active. On 24 March, ten M-class and ten C–class solar flares were detected originating from the NOAA Active Region 13615 at solar latitude and longitude S13W13 (https://solarmonitor.org). This FD is associated with a complex eruption at the Sun originating from Active Region (AR) 13614, which occurred on the 23rd of March between 00:00 [UT] and 05:00 [UT], and which exhibited signs of a complex eruption. It was followed by a sympathetic eruption from AR 13615. These events generated an X1.1 flare at 00:58 [UT]. Fig. 4 shows the erupting signatures as observed by
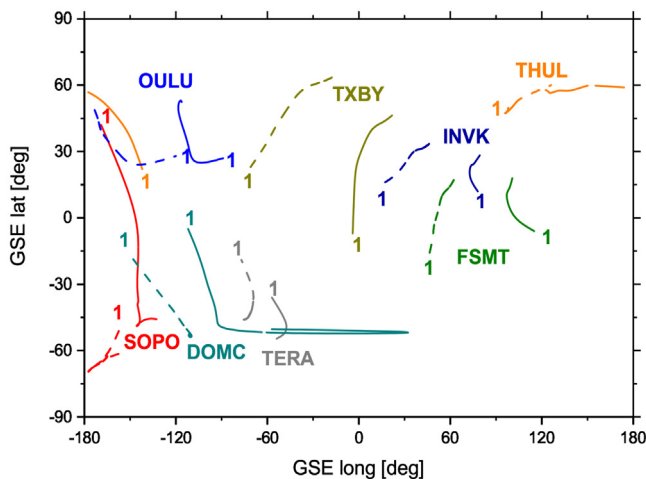
the Solar Dynamic Observatory (SDO) Atmospheric Imaging Assembly (AIA) Extreme Ultra-violet (EUV) filtergrams at 211Å and 304Å. As can be seen the north eruption (from AR 13614) was complex and with many phases that concluded with a distinct post-eruption arcade. The erupted structure at the peak of the eruption (2024–03-23T01:04 [UT]), indicated by the cyan arrows at the top row panels and the second panel of the bottom row of the same figure, has a unique shape that might be the result of different erupting structures. The sympathetic eruption from AR 13615 is indicated by yellow arrows on the last two panels of the top row images of the same figure. The two eruptions have different helicity sign and as they expand already in the low corona they will interact with each other resulting in possible deflections and/or reconnection. The CME white-light signatures generated by these event, as observed by the Solar and Heliospheric Observatory (SOHO) Large Angle and Spectrometric Coronagraph Experiment (LASCO) C2 coronagraph, are presented in Fig. 5. The light magenta arrow points to the leading shock that is driven in the corona by the eruption. Accordingly the light green arrow indicates the bright rim and trailing cavity of the associated CME. Following behind, already from 01:48 [UT] onwards, one can distinguish a second bright rim marked with a red arrow. This is considered to be a white-light signature supporting the idea of a second eruption.

Before the onset of Phase I of the FD, a strong magnetospheric compression took place in association with an interplanetary shock and CME arrival. It resulted in a sudden storm commencement at 14:34 UT on 24 March (www.obsebre.es).

As seen in Fig. 2, hourly averaged IMF strength reached its maximum at 19 UT and maximum solar wind speed at 21 UT (30.8 nT and 855 km s^{-1} respectively (https://omniweb.gsfc.nasa.gov/). Before the FD, the IMF B_z component was negative, with the lowest value of −15.8 nT at 15 UT, but during most of the event period, it was northward directed. The solar wind proton temperature reached a maximum value of about 1 MK. The maximum proton density was reached later, at 05 UT on 25 March.

Studies of the global, dynamical heliospheric situation with the ENLIL Model (Odstrčil et al., 1996) showed that the conditions around the Earth were strongly disturbed around the time of the FD. Fig. 6 shows two fast coronal mass ejections passing the Earth around 17:55 UT of 24 March. For the ENLIL modeling two CMEs were considered with Lon.=2.0°, Lat.=22.0°, Half Angle = 41.0° and Speed = 1613 km/s, and with Lon.=5.0°, Lat. = 5.0°, Half Angle = 45.0 ° and Speed = 1572 km/s.

Fig. 3. Asymptotic directions (in GSE coordinates) of selected polar NMs during Phase I (22 UT on 24-Mar-2024) - dashed lines and Phase II (01 UT on 25-Mar-2024) - solid lines, of the studied Forbush decrease. Locations of the NM acronyms denote the 20 GV rigidity end of the asymptotic direction, while the other end corresponds to the cutoff rigidity of 1 GV.
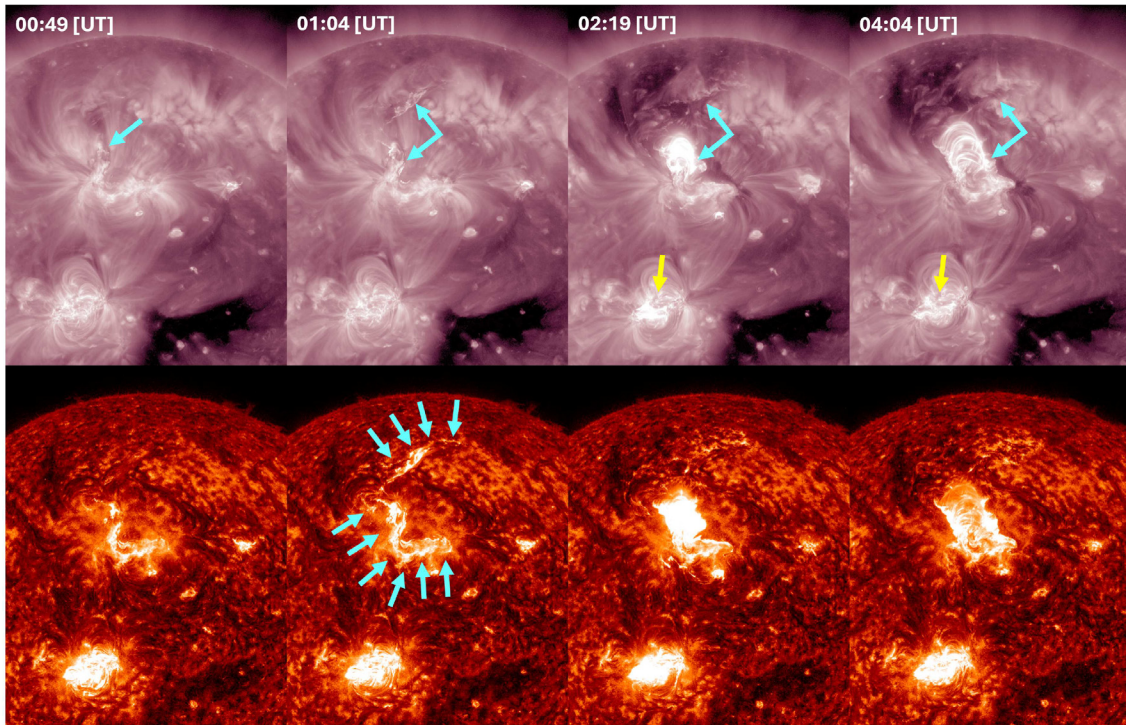
Fig. 4. Signatures of the eruption at the Sun as captured by SDO AIA EUV filtergrams at 211Å and 304Å. The cyan arrows in the top row panels and the second panel of the bottom row indicate the erupting signatures in EUV associated to the AR 13614. The yellow arrows on the top row indicate a sympathetic eruption launched by AR 13615.

Because of the FD's rapid recovery, we have also checked the space-borne records, specifically high-energy particle channels of the GOES data for a possible SEP event. During that time, there was only a slight increase in low-energy proton channels at $\geqslant 10$ and $\geqslant 50$ MeV, but not in a high-energy channel. We note that the very small increase in the > 100 MeV channel, which had a late onset, was probably due to shock acceleration. A detailed study is beyond the scope of this paper.

5. Analysis and discussion

5.1. Anisotropy

Because of the inclination of the Earth's axis with respect to the ecliptic and Earth's rotation, the geographical (GEO) coordinate projection of the asymptotic cones of NMs is not representative for the development of the event in interplanetary space. Here, we present maps, in GSE coordinates, of NM responses where the location and size of symbols correspond to the asymptotic directions at the geomagnetic cutoff rigidity P_c (or 1 GV for high-latitude NMs) and the magnitude of FD, for Phase I (Fig. 7) and Phase II (Fig. 8), respectively. Mid- and low-latitude NMs are denoted by blue circles, and high-latitude NMs by red circles.

We have tested the first-order fit to the anisotropy of data shown in Fig. 7 by assuming a linear sum of the iso-tropic and anisotropic components, the latter is represented by a Gaussian distribution on the celestial sphere so that the NM responses S are approximated by

$$S = M_0 + M_1 \cdot \exp\left(\frac{-R^2}{2\sigma^2}\right), \tag{1}$$

where M_0 is the isotropic component (in % of FD), M_1 is the magnitude of the anisotropic decrease (also in %), R is the angular distance from the anisotropy axis, and σ is the width of the anisotropy angular distribution in GSE coordinates. The fit was done by minimizing the RMSE (root mean square error) discrepancy between the NM responses modelled by the function S and the measured ones. The best-fit parameters for Phase I were found as $M_0 = 10$ %; $M_1 = 6$ %; $\sigma = 28°$; the location of the aniso-tropy axis has the latitude $2°$ and longitude $-136°$ in GSE coordinates. This is shown in Fig. 7 by the grey star and the 1σ contour. The best-fit parameters for Phase II are $M_0 = 8$ %; $M_1 = 12$ %; $\sigma = 18°$; the location of the ani-sotropy axis has the latitude $42°$ and longitude $-175°$ in GSE coordinates. It is interesting that this anisotropy is located in the anti-Sunward direction close to the ecliptic plane and has a narrow cone of anisotropy. The derived anisotropy, combined with additional heliospheric obser-vations and full modeling, could allow a comprehensive interpretation of this complicated event, which is beyond the focus of the present study and is planned as future work.
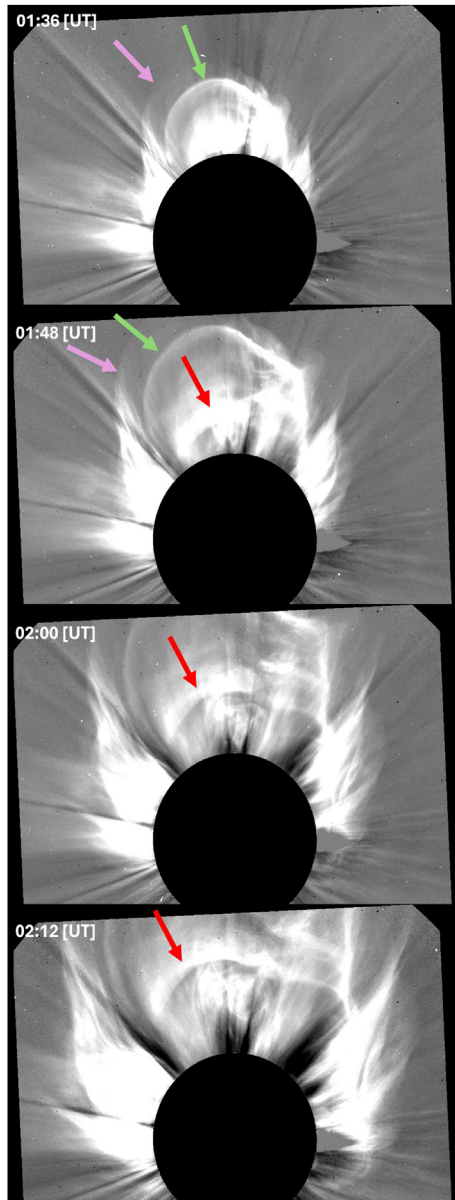
Fig. 5. White light signatures, from SOHO LASCO C2 coronagraph, associated with the eruptions presented in Fig. 4. The light magenta arrow indicates the shock generated by the first eruption, while the green arrow indicates the CME that drives this shock. The red arrow indicates the second CME signatures.

5.2. Dependence of decrease magnitude on the geomagnetic cutoff rigidity

The observed FD magnitude depends on the cutoff rigidity (e.g., Usoskin et al., 2008) which in turn defines the NM's effective energy E_{eff} (Asvestari et al., 2017) as shown in Fig. 9. Because of the large spread of the FD magnitudes at low- and mid-cutoff NMs due to the anisotropy, we have combined them in 2-GV-wide bins as indicated by red crosses in the Figure. The data were formally fit, using the χ^2 metrics, by exponential and power-law functions as indicated in the Figure caption.

We note that the 2-GV bins allowed us unbiased analysis, because of the smoothed NM response. We emphasize that this two-phase event looks slightly different from the bulk of FDs. On the other hand, an unambiguous interpretation and comparison with other events requires more detailed modeling considering explicitly the available heliospheric data, which is beyond the scope of this phenomenological paper.

5.3. Temporal variation of the cosmic ray spectrum

A classic indicator of spectral evolution is to compare the count rate vs. time from neutron monitors at different cutoff rigidities (Fig. 1).

In addition to standard NMs, which are most sensitive to secondary neutrons with energies from ∼10 MeV to ∼10 GeV in cosmic-ray induced atmospheric showers (Aiemsa-ad et al., 2015), some stations around the world also deploy bare neutron counters without the lead producer or polyethylene reflector, which are more sensitive to atmospheric neutrons of much lower energy, and hence are relatively more sensitive to primary cosmic rays of lower rigidity (Nuntiyakul et al., 2018; Nuntiyakul et al., 2020). Thus the bare/NM count rate ratio has been used as an indicator of the spectral index, especially for GLE events (Bieber and Evenson, 1991; Bieber et al., 2004; Ruffolo et al., 2006; Bieber et al., 2013).

More recently, neutron time delay distributions from a single NM have been used to extract the leader fraction, *L*, i.e., the fraction of neutron counts that did not follow another count associated with the same cosmic ray shower (Ruffolo et al., 2016; Banglieng et al., 2020). Using data collected during latitude surveys, the leader fraction has been shown to serve as another indicator of the cosmic ray spectral index (Mangeard et al., 2016). Note that the absolute magnitude of *L* depends on the station altitude, e.g., the sea level MWSN has a higher value than PSNM and SOPO at high altitude. (The magnitude of *L* also depends on the cutoff rigidity, dead time, and data acquisition system.) As seen in Fig. 10, for the FD starting on 24 March 2024, the bare/NM count rate ratio and leader fraction data from various stations indicate spectral changes or a lack thereof in different rigidity ranges.

The cosmic ray spectrum at each time can be roughly represented by a power law, at least over a limited rigidity range, i.e., the flux can be characterized as $j \propto P^{-\gamma}$, where γ is a spectral index. Muangha et al. (2023) reported a relationship between the South Pole leader fraction, *L*, and γ as inferred from daily AMS-02 proton observations (Aguilar et al., 2021b) over the range of 2.97 to 16.6 GV:

$$\gamma = -36.47 + 51.48 \cdot L. \qquad (2)$$

The variability of the leader fraction at different NMs during the FD is shown in Fig. 10 and exhibits a significant decrease during the deep phase of the event. The observed change in the South Pole *L* by $\Delta L \approx -0.006$ implies, using the relation above, a change in γ by -0.31 for cosmic ray
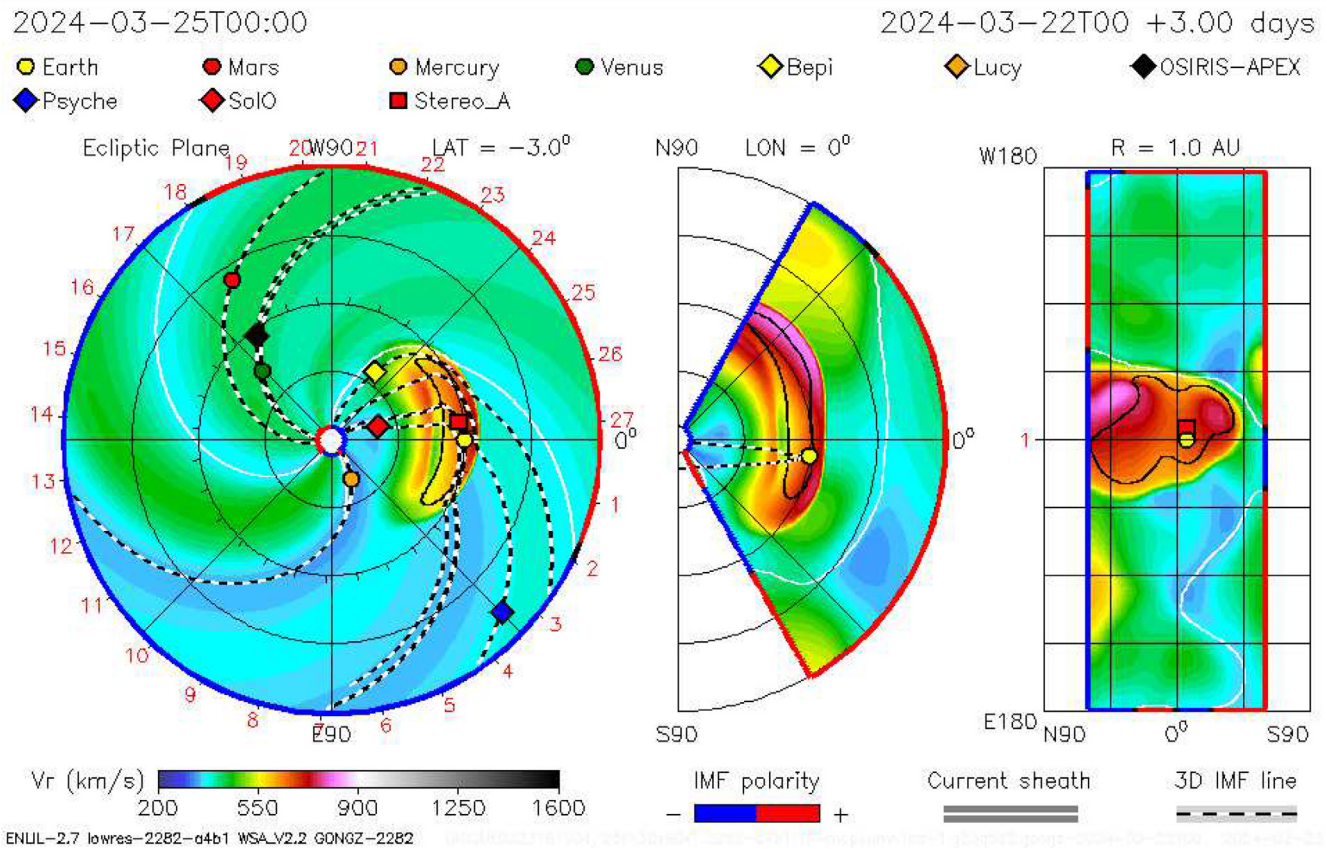
Fig. 6. Radial solar wind velocity contour plots shown in the ecliptic (left panel), meridional (middle panel), and radial (right panel) planes for 25 March 2024 at 00:00 UT (source: https://ccmc.gsfc.nasa.gov/).
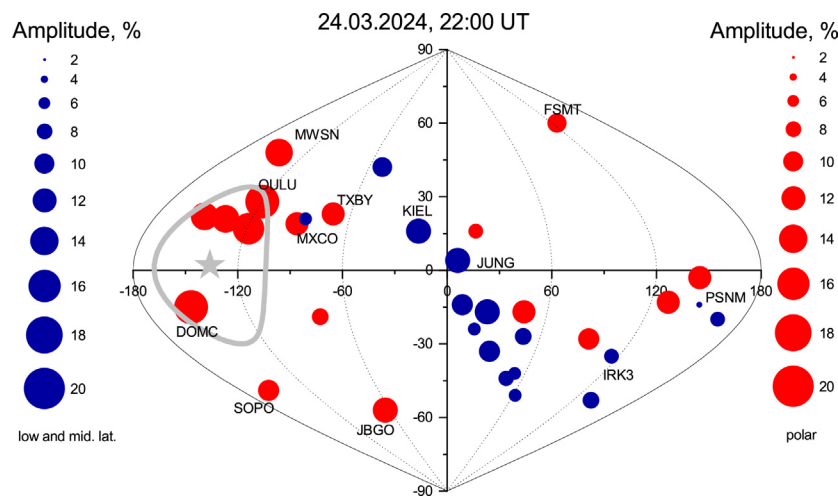

Fig. 7. Map (sinusoidal projection, GSE coordinates) of the NM asymptotic directions and FD responses at polar ($P_c < 1$ GV – red circles) and other (blue circles) NMs. The size of the symbol represents the maximal amplitude of the Forbush decrease observed by the corresponding station during Phase I (24 March 2024, 22:00 UT). The grey star and contour depict the centre and 1σ width of the anisotropy.

protons of that rigidity range. The fact that the FD appears stronger at lower rigidity implies that the cosmic ray spectrum hardens (flattens) during the deep phase, i.e., its spectral index decreases.

Note also that according to Fig. 10, on March 25 the indicators of the spectral index rapidly returned back (within a few hours) to the pre-event trend, while the count rates took several days to recover. This indicates that the
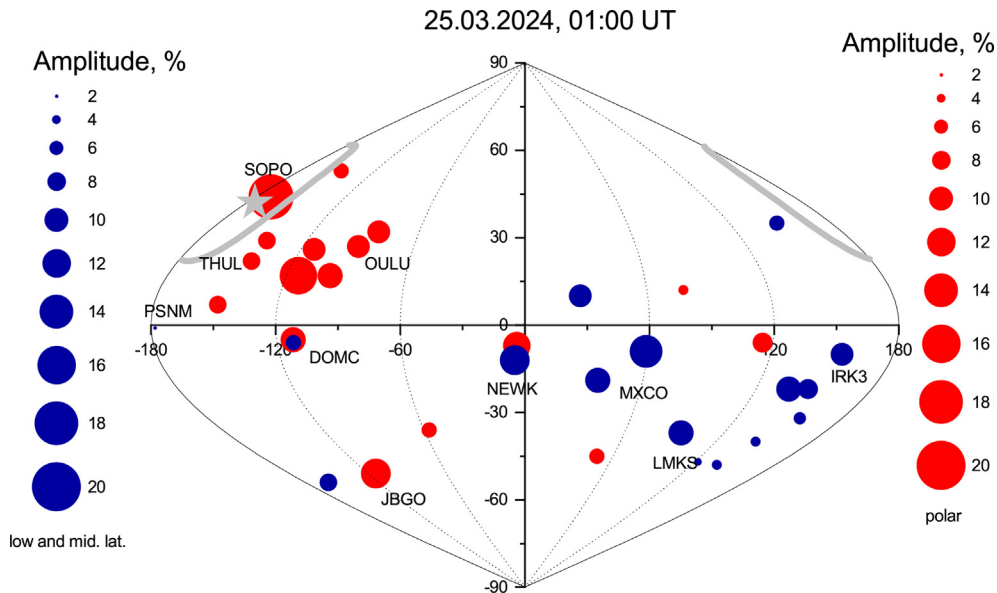
Fig. 8. The same as Fig. 7 but for Phase II (25 March 2024, 01:00 UT).
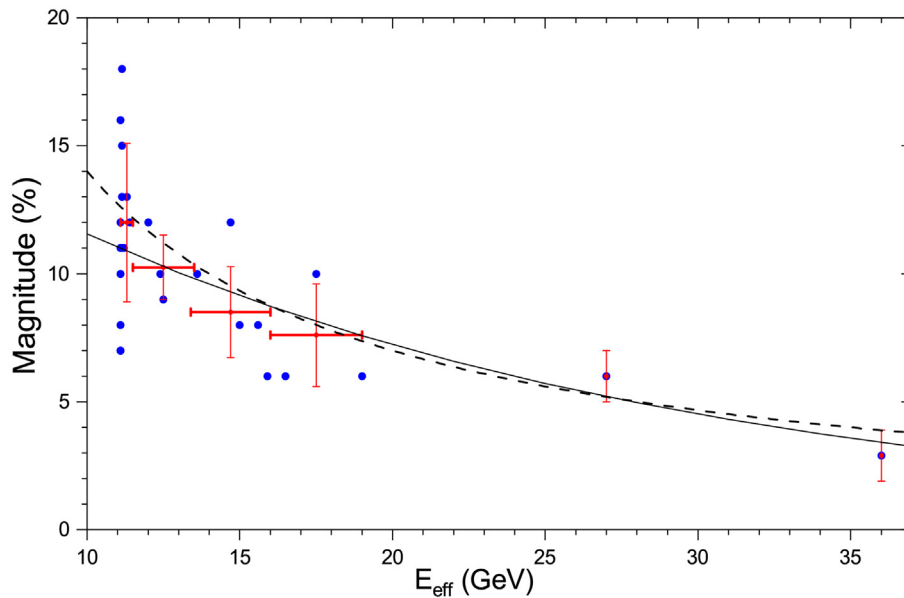
Fig. 9. Maximum magnitude (in %) of the Forbush decrease as a function of the effective energy E_{eff} (as defined in Asvestari et al., 2017) of the NMs studied here. Blue dots depict values for individual NMs, and red crosses show averaged values over 2-GV bins. The solid and dashed lines depict the best-fit exponential $\left(M = (18.5 \pm 3.5) \cdot \exp((-0.047 \pm 0.010) \cdot E_{\text{eff}})\right)$ and power-law $\left(M = (140 \pm 60) \cdot E_{\text{eff}}^{-1.0 \pm 0.1}\right)$ functions, respectively.

recovery phase of the FD was rigidity-independent and had essentially the same spectral shape as the pre-event period, despite the lower flux level.

It is interesting to compare the changes in the leader fraction L for the SOPO NM for this event with those reported for other moderate FD events in the previous solar cycle during Nov 2014 and Jun 2015 (both $\approx$10% magnitude) as reported by Banglieng et al. (2020). The corresponding leader fraction changes ΔL were about -0.003 during Nov 2014, -0.0025 during June 2015, and -0.006 during March 2024. Therefore, the change in the SOPO

L, and hence the change in the proton spectral index γ over about 3 to 17 GV, was roughly proportional to the magnitude of the FD decrease for all three events.

On the contrary, the leader fraction at PSNM, which has the world's highest vertical cutoff rigidity of $\approx$17 GV, remained unchanged throughout the FD studied here, within the daily uncertainty of $\approx$ 0.0002. This is in contrast with the changes in PSNM L during previously studied FDs in Nov 2014 by ≈ -0.0007 and in Jun 2015 by ≈ -0.0006 (Banglieng et al., 2020). (For comparison, note that the long-term variation in PSNM L throughout Solar
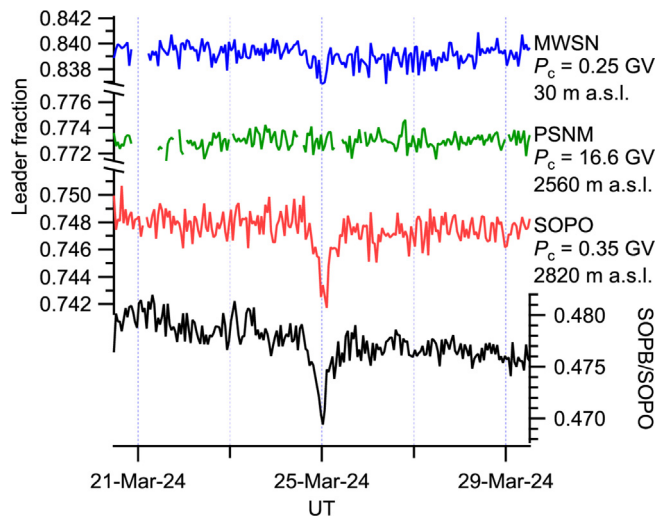
Fig. 10. Indicators of changes in the cosmic ray spectrum during the FD using time series of hourly data from selected NM stations. Top: Leader fraction, which serves as an indicator of the spectral index, from MWSN, PSNM, and SOPO. Bottom: The count rate ratio between bare counters and a neutron monitor at the South Pole (SOPB/SOPO), another indicator of the spectral index. The decrease in the spectral index, i.e., hardening of the spectrum, is consistent with a much stronger Forbush decrease at lower cutoff rigidity. Note that on March 25 the spectral index rapidly rose back to the pre-event trend, while the count rates took several days to recover, indicating that the recovery phase had essentially the same spectral shape as the pre-event period. Note also that PSNM at cutoff rigidity ≈ 17 GV exhibited no clear change in the leader fraction, indicating that at high rigidity the spectral shape was unchanged throughout the event.

Cycle 24 was reported to be 0.0008.) The corresponding count rate FD magnitudes at PSNM were about 2.6% during Nov 2014, 3.7% during Jun 2015, and 3.6% during Mar 2024. Thus we see that the PSNM L can behave quite differently for different FDs of similar magnitude, as also reported by Ruffolo et al. (2016). For the event examined here, the lack of a measurable change in PSNM L indicates that the FD was essentially rigidity-independent at $\gtrsim 20$ GV. This suggests that the FD likely persisted to even higher rigidities. In other words, the leader fraction data from PSNM extend the "reach" of the NM network to rigidities beyond the maximum P_c value of ≈ 17 GV.

6. Conclusions

In this paper, we reported observational results from the global NM network, including count rates of NMs and bare neutron counters and neutron timing data, related to the registration of a highly anisotropic FD. The observed FD was quite unusual, first revealing a rapid and rigidity-independent recovery, secondly a strong anisotropy, and a notable temporal shift in NM responses. A careful and realistic modelling employing IGRF and Tsyganenko 01 models and explicitly considering the actual near space and geomagnetospheric conditions was carried out to account for the NM responses. It was shown that a narrow cone-like anisotropy was located nearly in the

anti-sunward direction close to the ecliptic plane, for both Phase I and Phase II of the studied event. This implies that the difference in the timing of the deepest phase of the FD as observed by different NMs was likely caused by the Earth's rotation so that the asymptotic directions of the NMs were moving in and out of the FD anisotropy cone.

It is speculated that the FD reported here could be a result of two interacting interplanetary CMEs (ICMEs), forming a complicated magnetic structure, accordingly causing the observed anisotropy. The hypothesis of two interactuating ICMEs is somehow supported by the observation in the Sun's corona and the ENLIL modelling, yet 1 AU data could be explained by a single shock and magnetic cloud event. Therefore, careful modelling of the interplanetary conditions and the ICMEs is necessary for a full understanding of this complicated event, which is beyond the scope of this phenomenological work.

Declaration of Competing Interest

The authors declare that they have no known competing financial interests or personal relationships that could have appeared to influence the work reported in this paper.

Acknowledgments

References

Adams, N., 1950. A temporary increase in the neutron component of cosmic rays. Phil. Mag. 41, 503–505.

Adriani, O., Barbarino, G., Bazilevskaya, G., et al., 2017. Ten years of PAMELA in space. Rivista del Nuovo Cimento 40 (10), 473–522. https://doi.org/10.1393/ncr/i2017-10140-x.

Aguilar, M., Ali Cavasonza, L., Ambrosi, G., et al., 2021a. The Alpha Magnetic Spectrometer (AMS) on the international space station: Part II - Results from the first seven years. Phys. Rep. 894, 1–116. https://doi.org/10.1016/j.physrep.2020.09.003.

Aguilar, M., Cavasonza, L.A., Ambrosi, G., et al., 2021b. Periodicities in the Daily Proton Fluxes from 2011 to 2019 Measured by the Alpha Magnetic Spectrometer on the International Space Station from 1 to 100 GV. Phys. rev. Lett. 127 (27), 271102. https://doi.org/10.1103/PhysRevLett.127.271102.

Aiemsa-ad, N., Ruffolo, D., Sáiz, A., et al., 2015. Measurement and simulation of neutron monitor count rate dependence on surrounding structure. J. Geophys. Res. 120, 5253–5265. https://doi.org/10.1002/2015JA021249.

Alanko, K., Usoskin, I.G., Mursula, K., et al., 2003. Heliospheric modulation strength: Effective neutron monitor energy. Adv. Space Res. 32, 615–620. https://doi.org/10.1016/S0273-1177(03)00348-X.

Alken, P., Thébault, E., Beggan, C.D., et al., 2021. International Geomagnetic Reference Field: the thirteenth generation. Earth Planet. Space 73 (1), 49. https://doi.org/10.1186/s40623-020-01288-x.

Asvestari, E., Gil, A., Kovaltsov, G.A., et al., 2017. Neutron monitors and cosmogenic isotopes as cosmic ray energy-integration detectors: effective yield functions, effective energy, and its dependence on the local interstellar spectrum. J. Geophys. Res. (Space Phys.) 122, 9790–9802. https://doi.org/10.1002/2017JA024469.

Banglieng, C., Janthaloet, H., Ruffolo, D., et al., 2020. Tracking cosmic-ray spectral variation during 2007–2018 using neutron monitor time-delay measurements. Astrophys. J. 890 (1), 21. https://doi.org/10.3847/1538-4357/ab6661.

Belov, A., 2009. Forbush effects and their connection with solar, interplanetary and geomagnetic phenomena. Proc. Int. Astron. Union 4 (S257), 439–450. https://doi.org/10.1017/S1743921309029676.

Bieber, J.W., Clem, J., Evenson, P., et al., 2013. Giant Ground Level Enhancement of Relativistic Solar Protons on 2005 January 20. I. Spaceship Earth Observations. Astrophys. J. 771, 92. https://doi.org/10.1088/0004-637X/771/2/92.

Bieber, J.W., Evenson, P., 1991. Determination of Energy Spectra for the Large Solar Particle Events of 1989. In International Cosmic Ray Conference (p. 129). volume 3 of International Cosmic Ray Conference.

Bieber, J.W., Evenson, P., Dröge, W., et al., 2004. Spaceship Earth Observations of the Easter 2001 Solar Particle Event. Astrophys. J. Lett. 601, L103. https://doi.org/10.1086/381801.

Bütikofer, R., 2018. Ground-based measurements of energetic particles by neutron monitors. In: Solar Particle Radiation Storms Forecasting and Analysis, The HESPERIA HORIZON 2020 Project and Beyond chapter 6. Springer Nature, Cham, Switzerland, pp. 95–112.

Cane, H.V., 2000. Coronal Mass Ejections and Forbush Decreases. Space Sci. Rev. 93, 55–77. https://doi.org/10.1023/A:1026532125747.

Desai, M., Giacalone, J., 2016. Large gradual solar energetic particle events. Liv. Rev. Solar Phys. 13, 3. https://doi.org/10.1007/s41116-016-0002-5.

Dorman, L., 2004. Cosmic Rays in the Earth's Atmosphere and Underground. Kluwer Academic Publishers, Dordrecht.

Dumbović, M., Vršnak, B., Temmer, M., et al., 2022. Generic profile of a long-lived corotating interaction region and associated recurrent Forbush decrease. Astron. Astrophys. 658, A187. https://doi.org/10.1051/0004-6361/202140861, arXiv:2201.09623.

Forbush, S., 1937. On the effects in cosmic-ray intensity observed during the recent magnetic storm. Phys. Rev. 51 (12), 1108–1109.

Gaisser, T., Engel, R., Resconi, E., 2016. Cosmic Rays and Particle Physics. Cambridge University Press, Cambridge, UK.

Gil, A., Usoskin, I.G., Kovaltsov, G.A., et al., 2015. Can we properly model the neutron monitor count rate? J. Geophys. Res. 120, 7172–7178. https://doi.org/10.1002/2015JA021654.

Gopalswamy, N., Barbieri, L., Cliver, E., et al., 2005. Introduction to violent sun-earth connection events of October-November 2003. J. Geophys. Res.: Space Phys. 110 (A9), A09S00. https://doi.org/10.1029/2005JA011268.

Hatton, C.J., Carmichael, H., 1964. Experimental Investigation of the NM-64 Neutron Monitor. Canad. J. Phys. 42, 2443–2472. https://doi.org/10.1139/p64-222.

Klein, K.-L., Dalla, S., 2017. Acceleration and Propagation of Solar Energetic Particles. Space Sci. Rev. 212, 1107–1136. https://doi.org/10.1007/s11214-017-0382-4, arXiv:1705.07274.

Kuwabara, T., Bieber, J., Clem, J., et al., 2006a. Development of a ground level enhancement alarm system based upon neutron monitors. Space Weather 4 (10), S10001. https://doi.org/10.1029/2006SW000223.

Kuwabara, T., Bieber, J., Clem, J., et al., 2006b. Real-time cosmic ray monitoring system for space weather. Space Weather 4 (8). https://doi.org/10.1029/2005SW000204.

Kuwabara, T., Bieber, J., Evenson, P., et al., 2009. Determination of interplanetary coronal mass ejection geometry and orientation from ground-based observations of galactic cosmic rays. J. Geophys. Res.: Space Phys. 114 (5). https://doi.org/10.1029/2008JA013717.

Larsen, N., Mishev, A., Usoskin, I., 2023. A New Open-Source Geomagnetosphere Propagation Tool (OTSO) and Its Applications. J. Geophys. Res. (Space Phys.) 128 (3). https://doi.org/10.1029/2022JA031061, e2022JA031061.

Mangeard, P.-S., Ruffolo, D., Sáiz, A., et al., 2016. Dependence of the neutron monitor count rate and time delay distribution on the rigidity spectrum of primary cosmic rays. J. Geophys. Res. (Space Phys.) 121 (A10), 11620. https://doi.org/10.1002/2016JA023515.

Mavromichalaki, H., Papaioannou, A., Plainaki, C., et al., 2011. Applications and usage of the real-time Neutron Monitor Database. Adv. Space Res. 47, 2210–2222. https://doi.org/10.1016/j.asr.2010.02.019.

Mavromichalaki, H., Paschalis, P., Gerontidou, M., et al., 2024. An assessment of the gle alert++ warning system. Atmosphere 15 (3). https://doi.org/10.3390/atmos15030345.

Miroshnichenko, L.I., 2018. Retrospective analysis of GLEs and estimates of radiation risks. J. Space Weather Space Climate 8, A52. https://doi.org/10.1051/swsc/2018042.

Mishev, A., Poluianov, S., 2021. About the altitude profile of the atmospheric cut-off of cosmic rays: New revised assessment. Sol. Phys. 296 (8). https://doi.org/10.1007/s11207-021-01875-5.

Mishev, A., Usoskin, I., 2020. Current status and possible extension of the global neutron monitor network. J. Space Weather Space Climate 10. https://doi.org/10.1051/swsc/2020020.

Muangha, P., Ruffolo, D., Sáiz, A. et al., 2023. Comparison of Cosmic Ray Spectral Variation during 2015–2019 as Indicated by the South Pole Neutron Monitor Leader Fraction and AMS-02 Spectral Index. In: 38th International Cosmic Ray Conference (p. 1304).

Nuntiyakul, W., Mangeard, P.S., Ruffolo, D., et al., 2020. Direct determination of a bare neutron counter yield function. J. Geophys.

Res. (Space Phys.) 125 (4), e27304. https://doi.org/10.1029/2019JA027304.

Nuntiyakul, W., Sáiz, A., Ruffolo, D., et al., 2018. Bare neutron counter and neutron monitor response to cosmic rays during a 1995 latitude survey. J. Geophys. Res.: Space Phys. 123 (9), 7181–7195. https://doi.org/10.1029/2017JA025135.

Odstrčil, D., Smith, Z., Dryer, M., 1996. Distortion of the heliospheric plasma sheet by interplanetary shocks. Geophys. Res. Lett. 23, 2521–2524. https://doi.org/10.1029/96GL00159.

Potgieter, M., 2013. Solar Modulation of Cosmic Rays. Living Rev. Solar Phys. 10, 3. https://doi.org/10.12942/lrsp-2013-3, arXiv:1306.4421.

Reames, D.V. (2017). Solar Energetic Particles volume 932 of Lecture Notes in Physics. Berlin: Springer Verlag. doi:10.1007/978-3-319-50871-9.

Ruffolo, D., Sáiz, A., Mangeard, P.S., et al., 2016. Monitoring Short-term Cosmic-ray Spectral Variations Using Neutron Monitor Time-delay Measurements. Astrophys. J. 817 (1), 38. https://doi.org/10.3847/0004-637X/817/1/38.

Ruffolo, D., Tooprakai, P., Rujiwarodom, M., et al., 2006. Relativistic Solar Protons on 1989 October 22: Injection and Transport along Both Legs of a Closed Interplanetary Magnetic Loop. Astrophys. J. 639 (2), 1186–1205. https://doi.org/10.1086/499419.

Simpson, J.A., 1958. Cosmic radiation neutron intensity monitor. In: Annals of the Int. Geophysical Year IV, Part VII. Pergamon Press, London, p. 351.

Simpson, J.A., 2000. The Cosmic Ray Nucleonic Component: The Invention and Scientific Uses of the Neutron Monitor. Space Sci. Rev. 93, 11–32. https://doi.org/10.1023/A:1026567706183.

Simpson, J.A., Fonger, W., Treiman, S.B., 1953. Cosmic Radiation Intensity-Time Variations and Their Origin. I. Neutron Intensity Variation Method and Meteorological Factors. Phys. Rev. 90, 934–950. https://doi.org/10.1103/PhysRev.90.934.

Souvatzoglou, G., Papaioannou, A., Mavromichalaki, H., et al., 2014. Optimizing the real-time ground level enhancement alert system based on neutronmonitor measurements: Introducing gle alert plus. Space Weather 12 (11), 633–649. https://doi.org/10.1002/2014SW001102.

Tanabashi, M., Hagiwara, K., Hikasa, K., et al., 2018. Review of Particle Physics. Phys. Rev. D 3, 030001. https://doi.org/10.1103/PhysRevD.98.030001.

Tsyganenko, N., 2002. A model of the near magnetosphere with a dawn-dusk asymmetry. J. Geophys. Res.: Space Phys. 107 (A8). https://doi.org/10.1029/2001JA000219.

Usoskin, I.G., Braun, I., Gladysheva, O.G., et al., 2008. Forbush decreases of cosmic rays: Energy dependence of the recovery phase. J. Geophys. Res. 113, A07102. https://doi.org/10.1029/2007JA012955.

Väisänen, P., Usoskin, I., Mursula, K., 2021. Seven Decades of Neutron Monitors (1951–2019): Overview and Evaluation of Data Sources. J. Geophys. Res. (Space Phys.) 126 (5), e28941. https://doi.org/10.1029/2020JA028941.

Witasse, O., Sánchez-Cano, B., Mays, M., et al., 2017. Interplanetary coronal mass ejection observed at stereo-a, mars, comet 67p/churyu-mov-gerasimenko, saturn, and new horizons en route to pluto: Comparison of its forbush decreases at 1.4, 3.1, and 9.9 au. J. Geophys. Res.: Space Phys. 122 (8), 7865–7890. https://doi.org/10.1002/2017JA023884.